Feasibility of photoacoustic image guidance for telerobotic endonasal transsphenoidal surgery

Sungmin Kim, Youri Tan, Peter Kazanzides, and Muyinatu A. Lediju Bell

Abstract— Injury to the internal carotid arteries during the minimally invasive procedure to remove pituitary tumors (i.e., endonasal transsphenoidal surgery) could have many severe complications, including patient death. While preoperative CT or MR images are available to assist with navigation, the location of these arteries may be uncertain during surgery due to registration errors and intraoperative changes. Ideally, the surgeon should be able to visualize these arteries in real-time, even though they are behind the bone being drilled. We are therefore exploring the feasibility of a novel photoacoustic image-guided telerobotic system to measure the location of the artery with respect to the drill tip and to accurately visualize the spatial relationship between the artery and drill tip with respect to the imaging system components (i.e., the optical fiber attached to the drill and the ultrasound transducer). The potential system accuracy was evaluated in a two-stage approach that includes gross localization of the vessel center, followed by refinement with an image-based algorithm. This method was tested with a research-based da Vinci Surgical System, simulated photoacoustic data, and experimental data, revealing mean absolute errors of 1.89±0.93 mm and 0.3±0.2 mm for gross and fine positioning, respectively. Results are promising for surgeons to visualize the internal carotid arteries and thereby avoid injury with a teleoperative robotic approach.

I. INTRODUCTION

Pituitary tumors are commonly removed with the endonasal, transsphenoidal approach. To implement this procedure, surgical tools are passed through the nose, nasal septum, and sphenoid sinus, where sphenoid bone is drilled away to access and remove abnormal masses on the pituitary gland. This pea-sized gland is flanked by the internal carotid arteries, and accidental injury to these vessels is a serious surgical setback, resulting in extreme blood loss, thrombosis, delayed neurological deficits, stroke, and possibly death [1], [2].

While endoscopes or microscopes can provide real-time streaming video of anatomical structures, the visual information is limited to the superficial features, which are not always sufficient to recognize the location of the organs around the surgical area. In particular, an endoscope cannot detect whether an artery is located behind the bone being drilled. While existing navigation systems can be used to localize surgical instruments with respect to sub-surface anatomy, they suffer from inaccuracies in the registration between the preoperative image and the intraoperative coordinate frame.

To overcome this challenge, we are exploring the use of photoacoustic imaging to provide real-time monitoring during the drilling process. Light from a pulsed nanosecond

Authors are with the Department of Computer Science, Johns Hopkins University, Baltimore, MD 21218, USA. sungminkim@jhu.edu, pkaz@jhu.edu, mledijubell@jhu.edu

laser would be transmitted through a fiber. When tuned to a wavelength where the absorption of blood is higher than surrounding tissues and bone, this light will be preferentially absorbed by the carotid arteries, generating a pressure field that may be detected with an ultrasound probe. The fiber can be attached to or detached from the surgical drill, which can be hand-held or robotically controlled, and the ultrasound transducer can be placed externally on the temple of the skull surface to detect the generated acoustic waves [3]. An illustration of key anatomical features as they relate to the proposed imaging system design appear in our previous publication [3].

Our previous work in this area demonstrated the feasibility of using photoacoustic imaging to detect anatomic targets using this geometric arrangement of the laser and ultrasound probe, particularly in cases where conventional ultrasound imaging fails [4], [5]. In addition, contrast measurements were suggested to determine image-based features such as the amount of bone that remains to be drilled [6], the difference between proximal and distal vessel boundary visualization [3], and the energy and fluence required to visualize real blood hidden by bone [5]. We also developed and demonstrated a navigation system to guide the placement of the ultrasound probe so that its imaging plane intersects the tool-mounted laser path near the expected location of the carotid artery [7]. Limitations of this system, however, include the inability to remotely control the imaging system components during a minimally invasive procedure and the potential presence of photoacoustic signals wherever the light scatters after passing through bone and surrounding tissue. Thus, the presence of a photoacoustic signal does not necessarily indicate that a vessel is in the drill's path. A method to localize vessel centers with greater accuracy relative to the fiber axis is necessary, and implementing this in a teleoperative environment enables remote control of the system components.

This paper presents the feasibility of implementing our navigation system on a telerobotic platform, specifically, an "open source" research da Vinci [8]. In this setup, the surgeon sits at a master console and remotely controls three robot arms: one for the endoscope, one for the surgical drill (with optical fiber), and one for the ultrasound probe. In a conventional telesurgical setup, the surgeon would view the endoscope images on the master console. One novel feature of our system is the augmented visualization of the environment, based on different sources of information. In particular, the surgeon can visualize the spatial relationship between the ultrasound probe and drill, the preoperative CT image, the real-time photoacoustic image, and a guidance axis that is
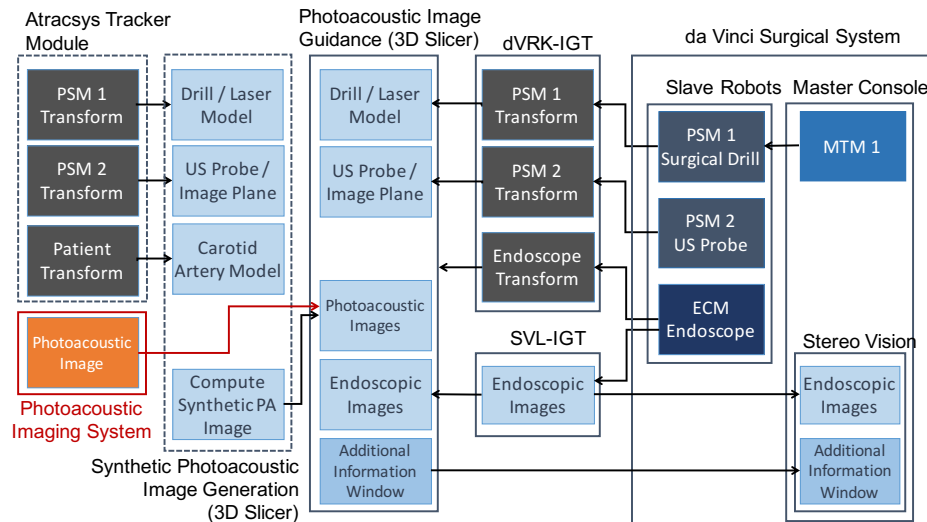
Fig. 1. System architecture for the proposed photoacoustic image guidance system for teleoperative surgery. Photoacoustic images are generated and sent to the Photoacoustic Image Guidance module (3D Slicer plug-in) for visualization, along with live stereo endoscope video (via SVL-IGT) and models of drill, laser, and US probe that are positioned based on kinematic position feedback from da Vinci PSMs (via dVRK-IGT). Visualizations from 3D Slicer are sent to the da Vinci stereo viewer. The dashed boxes represent modules that exist to generate simulated photoacoustic images for the gross-positioning experiments described in Section II.D.

designed to locate the cross-sectional center of the carotid artery. This paper presents the system architecture and the results of experiments that evaluate the system's ability to estimate the location of the critical carotid artery using a two stage approach that combines geometric and image-based information.

II. MATERIALS AND METHODS

A. Telerobotic System Overview

Our research testbed is based on the first generation da Vinci Surgical System, which can provide three patient side manipulators (PSMs) and one Endoscopic Camera Manipulator (ECM) on the patient side and two master tool manipulators (MTMs) for teleoperation at the master side. The manipulators are controlled by the open source da Vinci Research Kit electronics and software [8]. For this study, because the ultrasound probe, surgical drill, and endoscope are essential components of the navigation system and teleoperation is also required, two PSMs, an ECM, and a MTM for teleoperation of one of the PSMs are adopted. Fig. 1 presents a block diagram overview of the interface between the photoacoustic imaging system, the Photoacoustic Image Guidance System on 3D Slicer, and the da Vinci Surgical System. For the gross positioning experiments reported here, we employed simulated photoacoustic images, generated with an optical tracking system (Atracsys fusionTrack 500, Puidoux, Switzerland), as described in Section II.D.

The PSM1 instrument is used to represent the surgical drill for skull base surgery (as illustrated in Fig. 2) and it is assumed that the optical fiber for photoacoustic imaging would be mounted on this tool (the reported experiments used a standard da Vinci instrument instead of the surgical drill with optical fiber). To better emulate a surgical drill, we added a software feature to lock the end-wrist orientation
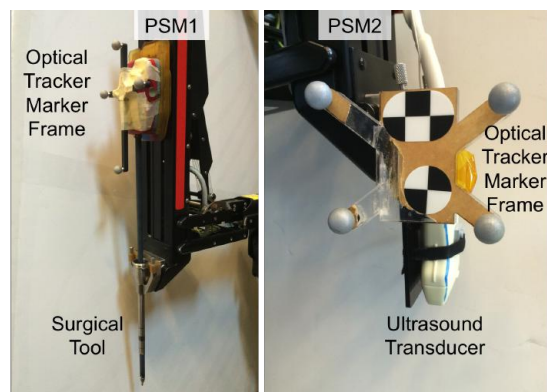

Fig. 2. Optically tracked markers attached to the surgical robot tool on PSM1 (left) and ultrasound transducer on PSM2 (right)

of the surgical instrument, since a drill would not provide those degrees of freedom (although this locking feature made teleoperation less intuitive). The ultrasound probe is installed on PSM2, which required modification of the original adaptor of the da Vinci System (as shown in Fig. 2). The right MTM is used to teleoperate PSM1.

The interface between the workstation and the research da Vinci Surgical System is based on the *cisst* library, with use of the Surgical Assistant Workstation (SAW) [9] and Robot Operating System (ROS) [10] interfaces. Moreover, the OpenIGTLink protocol is used to transfer kinematic data for PSM1, PSM2, and the ECM to other modules in this study.

The PSMs and ECM consist of a passive setup joint and an active arm. The setup joint is passively manipulated to adjust the position and orientation of the active arm for teleoperation. This system included a prototype interface between the da Vinci Research Kit electronics and the passive setup joints so that the software could obtain the position and orientation

of each setup joint.

For this study, the tool tip position and tool orientation are obtained via the kinematics of each arm, including both the passive setup joints and active manipulator. Due to the long kinematic chains, the system is not expected to have high accuracy, which is our primary motivation for using a photoacoustic image guidance system to estimate vessel centers. We expect that this approach should provide accurate measurements of the location of blood vessels relative to the tip of the surgical drill, even when the overall system accuracy is low.

B. Photoacoustic Image Guidance System

The Photoacoustic Image Guidance System (PA-IGS) consists of the photoacoustic image guidance module on 3D Slicer and the Photoacoustic Imaging system (replaced by the Atracsys Tracker module for the experiments described in Section II.D). The photoacoustic image guidance module is implemented in Python as a plug-in module for 3D Slicer. This module has basic roles for visualization of the spatial relationships among the ultrasound probe, photoacoustic image, surgical drill, and laser path, based on kinematic information from the telerobotic system or optical tracker [7]. The ultrasound probe and ultrasound plane are represented by dimensionally accurate CAD models The surgical drill is represented by a standard Slicer locator model and the laser path is represented by a cone shape model that mimics a divergent laser beam with a numerical aperture of 0.37 (i.e., cone half angle of 16°, as illustrated in Fig. 3).

In addition, several assistant functions to operate with the telerobotic system are added in this study; the main functions provide various view layouts to provide pertinent information for the surgical procedures and to generate a guide axis to assist with teleoperation. For example, the PA-IGS has multiple views for display, including three slice views for the preoperative CT image, a photoacoustic image view, left and right endoscopic views, and two 3D views (free explore and surgical drill views). The 3D Slicer layout can be rearranged according to the surgical procedures and three different layout modes are provided: all views mode, photoacoustic image guidance mode, and stereoscopic surgery mode.

For teleoperation convenience, an additional information window is provided on the master console of the telerobotics system as a picture-in-picture view. The additional information window contains the photoacoustic image view, to determine whether or not the carotid artery signal is present (indicating that the artery is in the vicinity of the surgical drill), and a 3D surgical drill view. With this 3D view, the surgeon can also visualize the spatial relationship between the imaging plane and drill with respect to the patient.

The Stereo Endoscope Image Capturing Module acquires stereo images from the telerobotic system via an S-Video interface and displays the images on the master console. This module is implemented in C++ using the Stereo Vision Library (SVL) of the *cisst* libraries. Images are transferred to other modules via the OpenIGTLink network interface [11].
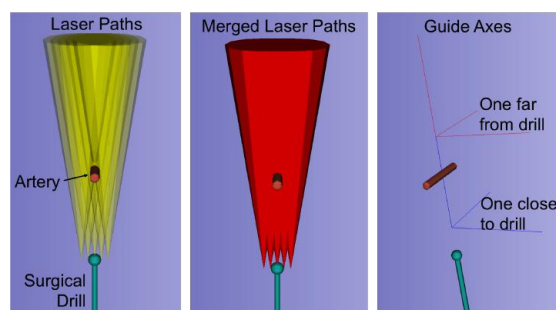

Fig. 3. The laser path model is accumulated when the photoacoustic image has a signal from the carotid artery (left), and the accumulated models are merged into a single model (center). Finally, the guide axes are determined by performing principal component analysis on the merged laser paths (right). Ideally, the guide axes should intersect the vessel, and any offset is considered a positioning error.
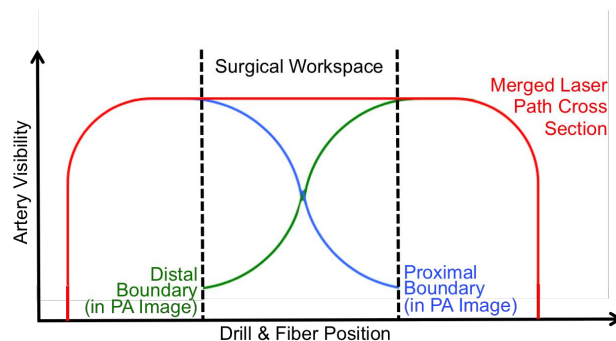

Fig. 4. Artery visibility during our two-stage approach as a function of the surgical drill and attached fiber position. Ideally, the first stage of our approach would be sufficient to determine the artery boundaries, but due to a limited surgical workspace, the boundary determined by the merged laser path cross section may not always be accurate. Therefore, the second stage of our approach is implemented by using photoacoustic images to visualize the proximal and distal vessel boundaries (relative to the ultrasound transducer). The intersection of these image-based boundaries is considered to be the vessel center.

C. Two-Stage Approach to Finding the Vessel Center

1) Geometry-Based Gross Positioning: It is difficult to determine the exact position of the carotid artery due to the divergent laser beam, as the photoacoustic image may indicate the presence of the carotid artery although it may not lie in the direct path of the cutter [3]. Thus, we propose an initial geometry-based approach to more accurately determine the location of the carotid artery, using polygonal models of the divergent laser beam.

To implement this approach, the surgeon would sweep the surgical drill in the sellar region of the surgical area [12] while watching the endoscopic images, the 3D surgical tool view, and the photoacoustic images. If the photoacoustic image indicates the presence of an artery, the tracing function for the laser path is enabled, and the PA-IGS module accumulates the laser path models that correspond to photoacoustic images containing the carotid artery, then the laser path model is displayed on the 3D view (Fig. 3-left). When the tracing function for the laser path is disabled, the accumulated laser path models are merged into a single model, as shown in Fig. 3-center. A Principal Component Analysis (PCA) is performed to find the principal axis of the merged laser path

model. Once this principal axis is determined, two guide axes along the same principal axis (i.e., one close to the drill, another one farther away from the drill) are displayed and the user teleoperates the surgical drill to align it with the guide axes. It is assumed that the principal axis corresponds to the central axis of the merged laser path model and, if the laser is swept across the entire carotid artery, a cross section of the merged laser path would ideally appear as shown in red in Fig. 4, and the center of this cross section should correspond to the center of the artery. This assumption is not always true, particularly if the laser beam path deviates from expected (which is very likely in the presence of light diffusion in tissue), the surgical workspace is limited (represented by the dashed lines in Fig. 4) and the carotid artery is always visible (i.e., represented by the flat region of the red curve located between the dashed lines in Fig. 4), or the tool is not translated in equal increments. These reasons necessitate a refinement step to localize vessel centers.

2) Fine Positioning with Image-Based Algorithm: For typical sizes of the carotid arteries (3.7-8.0 mm [13]), only the boundaries distal and proximal to the ultrasound transducer are expected to be visible in the photoacoustic images [3]. Therefore, using the photoacoustic data acquired during the gross positioning stage, one contrast measurement from each vessel boundary may be obtained from each photoacoustic image acquired as the fiber is translated, as indicated by the green and blue lines in Fig. 4. The difference between these two contrast measurements obtained from each photoacoustic image can then be used to update the location of the guide axis, placing it more accurately along the vessel center, or to estimate the surgeon's distance from the vessel center. The ability to make this distance estimate is particularly critical when diffusion of the light in the surrounding tissue causes the proximal or distal boundary to be present in a photoacoustic image although the fiber and surgical tool are not centered on or near either boundary.

D. Experiments to Test Gross Positioning

To test the first stage of our approach (i.e., gross positioning), we used a 3D-printed phantom (Fig. 5-left) that was created for our previous study [7]. This phantom has 5 square pillars of different heights, each used as a fiducial for registration. The top of each pillar has a hemi-spherical concavity to facilitate registration. The phantom is 60 x 25 x 25 mm and is fixed on a plastic container that is 100 x 60 x 100 mm. The dynamic reference base (DRB) is fixed on the surface of the plastic container, as shown in Fig. 5-left.

A cylindrical carotid artery model with a 4 mm diameter was virtually placed at one of three unique positions: center, left, and right, as shown in Fig. 5-right. Because the phantom does not contain a real structure for the carotid artery, it cannot be seen in the endoscopic images. This is consistent with the surgical procedure, where the carotid artery is behind the sphenoid bone and therefore not visible in the endoscopic images. It is possible, however, to observe the carotid artery model in the 3D view of 3D Slicer, which is available via the additional information window that is presented on the master console during the experimental procedure. This is analogous to an image-guided neurosurgical procedure, assuming that the carotid artery can be visualized in the preoperative image (e.g., in a preoperative MRI, or by estimating its location in a preoperative CT image based on other anatomical landmarks).

In addition to the DRB attached to the phantom, optical tracker marker frames were attached to the ultrasound transducer on PSM2 and the surgical instrument (representing the drill with a fiber attached) on PSM1, as shown in Fig. 2. The ECM and surgical tool on PSM1 were placed considering real clinical conditions, as shown in Fig. 6-left. Because the surgical drill has a narrow workspace during the endoscopic transnasal surgery, we limited robot movement to be within the front two pillars of the phantom, which are 25 mm apart.

The ultrasound transducer installed on PSM2 was additionally placed at an appropriate position to obtain simulated photoacoustic images of the carotid artery (see Fig. 6). The simulated photoacoustic images were generated by first using the optical trackers to determine the spatial relationship between the models of the ultrasound image plane, laser beam path, and carotid artery, as shown in Fig. 6-right. If the laser beam path model intersected the artery model, an intersection model obtained by using a boolean operation on these two polygonal models was generated. Then, the ultrasound image plane model was used to obtain a cross-section through this intersection model, resulting in a simulated photoacoustic image. The necessary geometric operations are provided by the Visualization Toolkit (VTK) [14]. The navigation software for placing the ultrasound transducer was described in our prior work [7].

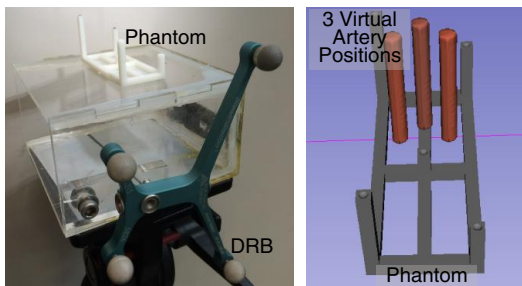Accuracy was determined by finding the carotid artery

Fig. 5. Phantom contains 5 square pillars of different heights, each used as a fiducial for registration (left), and the artery model is located at three different positions in the 3D view (right).
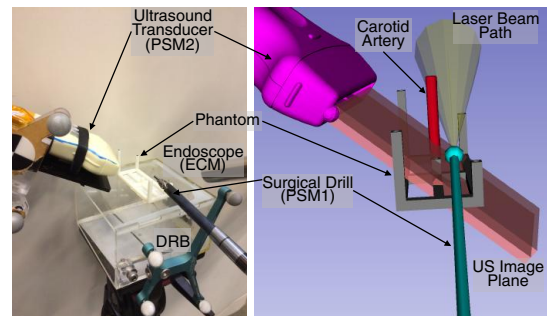

Fig. 6. Ultrasound transducer on PSM2, surgical drill on PSM1, and ECM arranged around phantom (left); visualization of experimental setup shown on 3D view of 3D Slicer (right).

using the simulated photoacoustic images, and then placing the drill so that its axis intersected the artery. Although this is counter to the clinical goal, which is to avoid the carotid artery, this evaluation provides quantitative evidence of the system accuracy and enables tabulation of two primary sources of error: (1) the measured distance between the robot tip and guide axis (i.e., measured by robot kinematics), and (2) the estimated distance between the guide axis and the artery. The second distance is estimated by subtracting the first distance from the total distance between the robot tip and the guide axis, as measured by the tracker. Note that the distance errors are one-dimensional. Three trials were performed for each artery location.

E. Experiments to Test Fine Positioning

The second stage of our approach (i.e., fine positioning) was tested using existing data acquired for and described in our previous publication [3]. To summarize the experimental procedure, a black, cylindrical, vessel-like target with a diameter of 3.5 mm and a 1 mm-thick bovine marrow bone cut to dimensions of 1.2 cm x 1.8 cm were embedded in a plastisol phantom during the phantom fabrication process. A 1 mm core diameter optical fiber (0.37 numerical aperture) was coupled to a 1064 nm Nd:YAG laser and affixed to a manual translation stage. The absence of optical or acoustic scatterers enabled visual alignment of the fiber with the center of the bone, vessel, and transducer, and the fiber was placed in this initial position, approximately 1 mm above the phantom surface. A cross-section of the phantom and experimental setup is illustrated in Fig. 7-left.

An Ultrasonix L14-5W/60 linear transducer (Richmond, BC, Canada) with a bandwidth of 5-14 MHz was placed with the long axis of the vessel perpendicular to the axial-lateral plane of the transducer. This transducer was connected to a SonixTouch ultrasound scanner, and a SonixDAQ data acquisition unit was triggered by the flashlamp output signal of the laser to access raw, pre-beamformed radiofrequency photoacoustic data. The fiber traversed the axial probe dimension, as indicated in Fig. 7-left, in approximately 0.3 mm increments from the initial position (i.e., the manual translation stage was calibrated in inches and converted to mm). The fiber traversed a total distance that was within the dimension limits of the sphenoid sinus [12]. Twenty images were acquired with each translation.
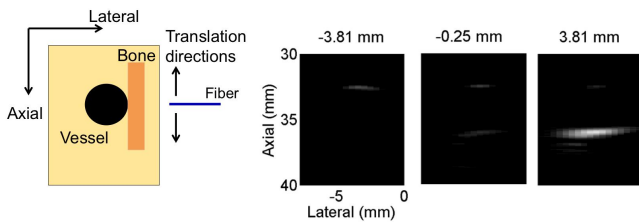

Fig. 7. Cross section of phantom and corresponding photoacoustic images of the proximal (left) and distal (right) and both (center) vessel boundaries as the fiber was translated by axial distance noted above each image (defined relative to the vessel center). The scale indicated in the left photoacoustic image applies to all images with distances defined relative to the transducer. All images are shown with 20 dB dynamic range.

Photoacoustic images (e.g., Fig. 7-right) were reconstructed with a delay-and-sum beamformer, and the resulting target contrast was measured as: $\text{Contrast}=20\log_{10}\left(\frac{S_i}{S_o}\right)$, where S_i and S_o are the means of the image data within regions of interest (ROIs) located inside and outside of the target, respectively. Two ROIs were defined in one image by searching for the maximum signals within the expected proximal and distal boundary locations, surrounding each signal with a 0.4 mm (axial) x 1.9 mm (lateral) rectangle, and automatically creating same-sized noise ROIs at the same depths, located approximately 1 mm from the left edge of the signal ROIs. All subsequent images used the same ROI positions. All data processing and analyses for this experiment were performed with MATLAB.

III. RESULTS

A. Teleoperation, Gross Positioning, and System Accuracy

Distance and angular errors for the first stage of our approach are presented in Table I. The teleoperation error (i.e., the error due to teleoperation with visual guidance) represents the distance between the robot tip and guide axis, as the goal was to place the robot tip along the guide axis. This error ranges from 0.03 mm to 2.29 mm with a mean $\pm$ one standard deviation of 1.18 $\pm$ 0.79 mm. The final column of Table I shows the angular teleoperation error (i.e., angular error between the robot tip and guide axis), which ranges from 4.27° to 7.19° with a mean $\pm$ one standard deviation of 5.30 $\pm$ 0.87°.

The gross positioning error represents the estimated distance between the guide axis and the artery center, which quantifies the accuracy of using the series of swept simulated photoacoustic images to localize the center of the carotid artery. These errors range from 0.29 mm to 2.97 mm with a mean $\pm$ one standard deviation of 1.89 $\pm$ 0.93 mm.

The overall system accuracy represents the distance between robot tip and artery center, which is measured by the Atracsys tracker position coordinates from the PSM1 (i.e., surgical tool) and the DRB. This measurement is considered as the ground truth, and it is the total distance accuracy of our system. For the nine trials, this accuracy ranges from 0.21 to 3.04 mm with a mean $\pm$ one standard deviation of 1.27 $\pm$ 0.91 mm. This accuracy is often lower than the teleoperation error or the gross positioning error due to error cancellation.

B. Fine Positioning Accuracy

The large distance errors reported in Table I motivate the purpose of the refinement step of our two-stage approach, which is to reduce errors with an image-based method that relies on contrast measurements from photoacoustic images acquired during the gross positioning stage of the approach. One example of such measurements is shown in Fig. 8-top, along with cubic polynomials for the best fit curves to these contrast measurements as a function of fiber position. In this example, the polynomial curves intersect at a value of -0.13 mm (i.e., the contrast difference is equal to zero at this distance from the manually determined vessel center). A total

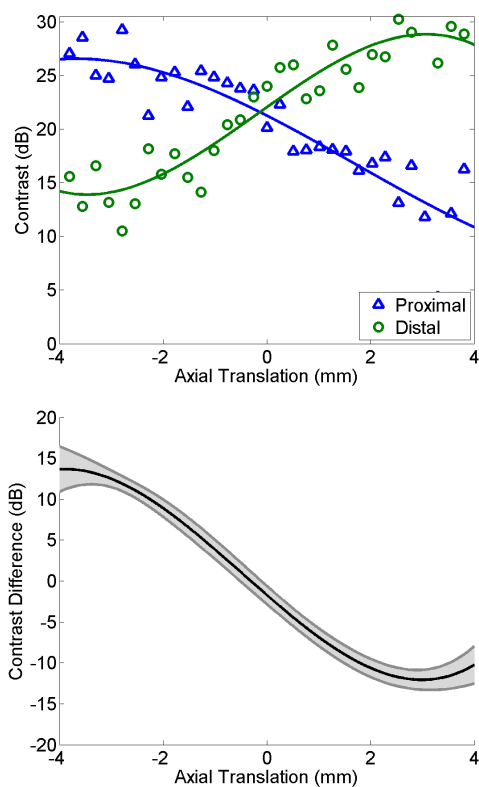| Artery Position | Trial # | Distance Errors | | | Angular Errors |
		Teleoperation Error (mm)	Gross Positioning Error (mm)	Overall (mm)	Teleoperation Error (°)
Center	1	2.29	2.08	0.21	7.19
	2	1.61	2.59	0.98	4.27
	3	0.03	2.14	2.11	4.52
Left	1	0.86	0.48	0.38	4.59
	2	0.29	1.60	1.89	5.59
	3	0.66	2.37	3.04	5.17
Right	1	1.28	0.29	0.99	5.32
	2	1.40	2.47	1.08	5.34
	3	2.27	2.97	0.80	5.72
Mean		1.18	1.89	1.27	5.30
Standard Deviation		0.79	0.93	0.91	0.87

Fig. 8. (top) Contrast measurements as a function of fiber translation for one image (out of twenty) acquired at each fiber position. The measurements were fit to cubic polynomials. The proximal and distal best fit line pairs from twenty such plots were averaged and subtracted from each other to achieve the mean contrast difference plot (bottom), with shaded error bars showing ± one standard deviation.

of twenty pairs of polynomial curves were fit to the acquired data.

The mean difference in contrast measurements (after fitting each pair of twenty contrast vs. translation curves to cubic polynomials) is shown in Fig. 8-bottom as a function of the known fiber translation, with shaded error bars representing ± one standard deviation. In general, the difference is approximately 0 dB when the fiber is centered on the vessel (i.e., 0 mm translation), positive for translations toward the probe, and negative for translations away from the probe. The value that intersects a contrast difference of 0 dB can be assumed as the true vessel center. This intercept occurs at a fiber position of -0.31 ± 0.2 mm from the visually determined vessel center, with values that ranged from -0.6 mm to 0.28 mm for the twenty cubic polynomial pairs.

IV. DISCUSSION

To the author's knowledge, this study is the first to report on a telesurgical photoacoustic image-guided navigation system setup, which was implemented on a research da Vinci System. This setup builds on our benchtop photoacoustic navigation system setup with handheld and optically tracked instruments [7]. A telerobotic approach is more ideal for minimally invasive surgeries and a multi-arm robotic system (as provided by the da Vinci System) utilizes continuously active robot-based kinematic chains to calibrate the location of the fiber relative to the ultrasound transducer (rather than rely on the tracker-based kinematic chains described in our previous work [7]). In addition, this work considers challenges introduced by the divergence of the laser beam, which were not addressed in our previous publication [7]. The updates herein required the addition of a software module to accumulate laser path models, extract a guide axis that visually indicates the location of the carotid artery, and incorporate photoacoustic images to refine localization of vessel centers, thereby providing more accurate guidance during teleoperation.

Potential sources of error for the gross positioning step include uneven sweeping of the surgical drill across the carotid artery and teleoperation delay. The accuracy of the guide axis can be guaranteed if the accumulated model is symmetric about the artery, thus evenly sweeping across the artery is essential, although difficult to perform in the experimental setup and most likely impossible to achieve in a clinical scenario due to motion limitations. We therefore introduce the fine positioning, image-based refinement step to compensate for the gross positioning errors. One source of error for this second step is fluctuations in laser energy, which provides varying contrast measurements for the same fiber position. As a result, as shown in Fig. 7, the images for 0 dB contrast

difference were often offset from the visually determined vessel center, which contributes to the 0.28-0.60 mm absolute range reported for this experiment.

Comparing Fig. 8-bottom to Fig. 8 in Ref. [3], we see that the introduction of the cubic polynomial fit in this publication significantly reduces the error of contrast differences from the same contrast measurements. The low standard deviation (e.g., 0.2 mm for 0 dB contrast difference) indicates that as many as twenty image acquisitions may not be necessary for reducing variations when the measurements are fit to cubic polynomials.

The results additionally showed relatively large teleoperation errors, which were greater than the minimum 1 mm distance separating the pituitary gland from the internal carotid arteries [15]. In the future, these errors could be significantly reduced by implementing a guidance virtual fixture on the master console. The angular errors are less of a concern if the artery is located close to the tool tip, which is the most critical surgical scenario.

The surgeon can use the displayed position of the carotid artery (i.e., the guide axis) to decide the best drilling path that avoids this critical structure. In an actual clinical scenario, there are two carotid arteries, thus the best drilling path may be the one that is centrally located between these two arteries, which would ideally be visualized in a single photoacoustic image. To achieve this goal, a larger surface area of incident light would be required, which might be preferred considering our recent report on the energy requirements for the visualization of real blood in the presence of bone [5]. In this scenario, the errors achieved with the two-stage approach are certainly sufficient, as they are an order of magnitude less than the 4 mm minimum separation distance between the carotid artery and the midline within the sellar region [12] (e.g., 8 mm minimum distance between carotid arteries). Our future work will therefore test this setup in a single experiment that combines a mobile photoacoustic imaging system with teleoperation.

V. CONCLUSION

Experiments were conducted to evaluate the feasibility and accuracy of visualizing the center of the carotid artery with a telerobotic system. The experiments were designed to confirm whether or not the developed system works smoothly in simulated conditions, the newly implemented functions (such as the determination of the guide axis and the image-based refinement approach) meet the functional requirements, and the resulting performance is acceptable for endonasal transsphenoidal surgery (and skull base surgery in general).

The experimental procedure first simulated the process of using photoacoustic imaging to find the carotid artery before or during the drilling operation. Specifically, the drill approaches the surgical area through the nasal cavity and is swept across the surface to obtain a series of photoacoustic images, which are then processed to present a guide axis that indicates the estimated location of the carotid artery. The experiments demonstrated that the system worked as desired. After this gross positioning step, the refinement step

was tested with existing experimental data to determine the location of the vessel center based solely on image contrast.

The proposed method is promising for surgeons to visualize carotid arteries, estimate proximity, and thereby avoid injury. Notably, the refinement step of this novel method to find the vessel center has promising potential in both a teleoperative environment, as well as an environment with alternative or minimal to no robotic assistance.

VI. ACKNOWLEDGMENTS

REFERENCES

[1] M. Perry, W. Snyder, and E. Thal, "Carotid artery injuries caused by blunt trauma." *Annals of Surgery*, vol. 192, no. 1, p. 74, 1980.

[2] J. Raymond, J. Hardy, R. Czepko, and D. Roy, "Arterial injuries in transsphenoidal surgery for pituitary adenoma; the role of angiography and endovascular treatment." *American Journal of Neuroradiology*, vol. 18, no. 4, pp. 655–665, 1997.

[3] M. A. Lediju Bell, A. K. Ostrowski, K. Li, P. Kazanzides, and E. M. Boctor, "Localization of transcranial targets for photoacoustic-guided endonasal surgeries," *Photoacoustics*, vol. 3, no. 2, pp. 78–87, 2015.

[4] M. A. Lediju Bell, A. K. Ostrowski, P. Kazanzides, and E. Boctor, "Feasibility of transcranial photoacoustic imaging for interventional guidance of endonasal surgeries," in *SPIE BiOS*, vol. 8943, pp. 894307–894307, Feb 2014.

[5] M. A. Lediju Bell, A. B. Dagle, P. Kazanzides, and E. Boctor, "Experimental assessment of energy requirements and tool tip visibility for photoacoustic-guided endonasal surgery," in *SPIE BiOS*, Feb 2016.

[6] M. A. Lediju Bell, A. K. Ostrowski, K. Li, P. Kazanzides, and E. Boctor, "Quantifying bone thickness, light transmission, and contrast interrelationships in transcranial photoacoustic imaging," in *SPIE BiOS*, pp. 93230C–93230C 2015.

[7] S. Kim, H. J. Kang, A. Cheng, M. A. Lediju Bell, E. Boctor, and P. Kazanzides, "Photoacoustic image guidance for robot-assisted skull base surgery," in *IEEE Intl. Conf. on Robotics and Automation (ICRA)*, May 2015, pp. 592–597.

[8] P. Kazanzides, Z. Chen, A. Deguet, G. S. Fischer, R. H. Taylor, and S. P. DiMaio, "An open-source research kit for the da Vinci® surgical system," in *IEEE Intl. Conf. on Robotics and Auto. (ICRA)*, Hong Kong, China, June 2014.

[9] P. Kazanzides, S. DiMaio, A. Deguet, B. Vagvolgyi, M. Balicki, C. Schneider, R. Kumar, A. Jog, B. Itkowitz, C. Hasser, and R. Taylor, "The Surgical Assistant Workstation (SAW) in minimally-invasive surgery and microsurgery," *Midas Journal*, Jun 2010. [Online]. Available: http://hdl.handle.net/10380/3179

[10] M. Quigley, K. Conley, B. Gerkey, J. Faust, T. B. Foote, J. Leibs, R. Wheeler, and A. Y. Ng, "ROS: an open-source Robot Operating System," in *IEEE Intl. Conf. on Robotics and Automation (ICRA), Workshop on Open Source Software*, 2009.

[11] J. Tokuda, G. S. Fischer, X. Papademetris, Z. Yaniv, L. Ibanez, P. Cheng, H. Liu, J. Blevins, J. Arata, A. J. Golby, T. Kapur, S. Pieper, E. C. Burdette, G. Fichtinger, C. M. Tempany, and N. Hata, "OpenIGTLink: an open network protocol for image-guided therapy environment," *Intl. J. of Medical Robotics and Computer Assisted Surgery*, vol. 5, no. 4, pp. 423–434, 2009.

[12] W. H. Renn and A. L. Rhoton Jr, "Microsurgical anatomy of the sellar region," *Journal of Neurosurgery*, vol. 43, no. 3, pp. 288–298, 1975.

[13] H. Takegoshi and S. Kikuchi, "An anatomic study of the horizontal petrous internal carotid artery: Sex and age differences," *Auris Nasus Larynx*, vol. 34, no. 3, pp. 297–301, 2007.

[14] C. Quammen, C. Weigle, and R. M. Taylor II, "Boolean Operations on Surfaces in VTK Without External Libraries," *MIDAS Journal*, May 2011. [Online]. Available: http://hdl.handle.net/10380/3262

[15] G. R. Isolan, P. H. P. de Aguiar, E. R. Laws, A. C. P. Strapasson, and O. Piltcher, "The implications of microsurgical anatomy for surgical approaches to the sellar region," *Pituitary*, vol. 12, no. 4, pp. 360–367, 2009.